Quasi–1D Anhydrite Nanobelts from the Sustainable Liquid Exfoliation of Terrestrial Gypsum for Future Martian-Based Electronics

Cencen Wei, Abhijit Roy, Adel K. A. Aljarid, Yi Hu, S. Mark Roe, Dimitrios G. Papageorgiou, Raul Arenal, and Conor S. Boland*

The sky is the limit with regards to the societal impact nanomaterials can have on the lives. However, in this study, it is shown that their potential is out of this world. The planet Mars has an abundant source of calcium sulfate minerals and in this work, it is shown that these deposits can be the basis of transformative nanomaterials to potentially support future space endeavors. Vitally, the methods applied are low cost and require no specialized instruments of great expertise, strengthening the potential involvement of nanotechnology in sustaining Martian inhabitation. Through a scalable eco-friendly liquid processing technique performed on two common terrestrial gypsum, this simple method presented a cost-efficient procedure to yield suspensions of large aspect ratio anhydrite nanobelts with long-term stability that are characterized through scanning electron microscopy and Raman spectroscopy. Transmission electron microscopy shows nanobelts to have a mesocrystal structure, with distinct nanoparticle constituents making up the lattice. Unexpectedly, anhydrite nanobelts have remarkable electronic properties, namely a bandgap that is easily tuned between semiconducting ($\approx$2.2 eV) and insulating ($\approx$4 eV) behaviors through dimensional control measured via atomic force microscopy. To demonstrate the application potential of the nanobelts; optoelectronic, electrochemical, and nanocomposite measurements are made.

1. Introduction

The study of nanomaterials, whether it be 1D nano-tubes[1] and -wires,[2] or 2D nanosheets,[3] has paved the way in advancing many crucial societal technologies. For a broad range of medical,[4] energy,[5] and optoelectronic applications,[6] these nanomaterials have brought about the realization of many Internet of Things devices. Recently, 2D nanosheets based on highly abundant, naturally occurring layered minerals were demonstrated to present many surprising properties. Micas and chlorite, from the phyllosilicate mineral family, when exfoliated down to low layer numbers displayed highly tunable electronic properties and unexpected catalytic capabilities.[7] This raises an interesting question of whether other common, abundant minerals could be exfoliated to yield new nanomaterial types that are also optimized for applications. If so, these nanominerals could be a potential source of research inspiration to further galvanize sustainable nanoscience investigations.

C. Wei, A. K. A. Aljarid, C. S. Boland
School of Mathematical and Physical Sciences
University of Sussex
Brighton BN1 9QH, UK
E-mail: c.s.boland@sussex.ac.uk
A. Roy, R. Arenal
Instituto de Nanociencia y Materiales de Aragon (INMA)
CSIC-Universidad de Zaragoza
Zaragoza 50009, Spain

A. Roy, R. Arenal
Laboratorio de Microscopias Avanzadas (LMA)
Universidad de Zaragoza
Calle Mariano Esquillor, Zaragoza 50018, Spain
Y. Hu, D. G. Papageorgiou
School of Engineering and Materials Science
Queen Mary University
London E1 4NS, UK
S. M. Roe
School of Life Sciences
University of Sussex
Brighton BN1 9QH, UK
R. Arenal
ARAID Foundation
Zaragoza 50018, Spain

One such common mineral of significant commercial interest is gypsum.[8] Globally, more than 150 million tons of gypsum was mined and processed in 2022[9] for a broad range of industries ranging from construction to food supplements.[10] In the United States alone, by 2033 the market size for gypsum is expected to be ≈$14 billion.[10] Nonetheless, gypsum in fact can be said to be so common, it has recently been discovered to even inhabit large areas of the Martian surface.[11] On Mars, gypsum is known to exist in large deposits, which are believed to contain most of the primordial water content of the planet.[12] With space exploration a buzz in recent years, humanity has set its sights on Mars as a potential destination. As such, many research has been undergone not only in the way of space travel logistics to our distant neighbor but also on how we might take advantage of the resources it has on offer to sustain human inhabitants. Naturally, one commodity of great interest is gypsum, with recent National Aeronautics and Space Administration (NASA)-funded research exploring modes in which the water content of gypsum may be extracted for human consumption.[13] Through a developed process, gypsum was dehydrated to form water vapor and waste material known as anhydrite. Specifically, anhydrite is the anhydrous phase of gypsum. However, we show here that this waste product could be applied to further sustain and support the future colonization of Mars. Intrinsically, it is known that gypsum minerals are made up of aggregates of amorphous nanobelts.[14] However, beyond understanding how the nanobelts form and coalesce into bulk minerals,[15] little materials science research has been performed on the individual properties of these nanostructures. By demonstrating the exciting potential anhydrite-based nanobelts possess, our work here presents a recourse in which Martian resources could be more fully utilized.

Using a green processing procedure, two forms of raw terrestrial gypsum minerals (selenite and satin spar) through a simple liquid-based dehydration procedure were converted to bassanite. These individual bassanite powders were then liquid phase exfoliated (LPE) in an aqueous medium to yield, regardless of gypsum source, suspensions of large aspect ratio anhydrite nanobelts. Through scanning electron microscopy (SEM), morphological changes occurring during each processing step were examined. We confirmed gypsum's conversion to its anhydrous nanobelt state and the nanobelts long-term stability against ambient reconversion to gypsum through Raman spectroscopy. Nanobelt lattice structure via transmission electron microscopy (TEM) was noted to be mesocrystalline and made up of nanoparticle segments with differing atomic planes. Through cascade centrifugation, suspensions of anhydrite nanobelts were separated into size fractions, revealing the nanobelts to possess bandgaps (E_g) as low as ≈2.2 eV. Additionally, due to quantum confinement effects in their smallest dimensions, nanobelt E_g rose to values of ≈4 eV as width and thickness controllably decreased. In application, anhydrite nanobelt networks displayed light-modulated current and catalytic performances for the hydrogen evolution reaction which surpassed many commonly applied nanomaterials. As a filler in a polymer matrix, low-loading levels of selenite anhydrous nanobelts displayed properties on par with other nano-reinforcers.

2. Results

2.1. Processing and Liquid Exfoliation of Gypsum

Commercially sourced bulk crystal variants of gypsum in the form of selenite and satin spar were procured as raw natural materials. In physical appearance, both minerals greatly differed, namely due to the mechanisms in which they formed. Gypsum minerals are known as evaporites,[16] whereby natural bodies of water high in calcium and sulfates have ions precipitate to form elongated bassanite nanoparticles ($CaSO_4 \cdot \frac{1}{2}H_2O$) ≈<10 nm in length via homogenous nucleation.[14,15,17] Bassanite nanoparticles then self-assemble to form precursor nanobelt templates that through heterogenous nucleation turn into gypsum nanobelts ($CaSO_4 \cdot 2H_2O$) in the presence of water.[15a,17] Through variations in growth conditions, tabular, like in the case of selenite, or fibrous, like satin spar, nanobelt aggregates are formed.[15b,18] From optical images of bulk selenite (**Figure 1a**) and satin spar (Figure 1b), the difference in growth structure is self-evident. Most noticeably, upon physical examination, was the difference in hue associated with the bulk crystals. For selenite, it had a light brown color. While satin spar was milky white and appeared chalky.

As the bulk crystals were raw minerals, a sustainable processing procedure (scheme in Figure 1c, see Experimental Section for more details) was applied to first clean them of surface contaminants and then powder them for liquid exfoliation. The procedure began by grinding the raw bulk minerals in a coffee grinder after that the ground powder was shear mixed in deionized water to remove water soluble contaminants. The resultant solution was then centrifuged, and the sediment taken forward to the next processing step. The next step was the ultra-sonication of a green solvent mixture of sediment in isopropanol (IPA),[19] where the solution was again centrifuged. The sediment was then collected and dried, to yield our clean powder. The clean powder then underwent LPE in an environmentally friendly water/sodium cholate surfactant solution[20] to yield in Figure 1d, high concentration (>6 mg mL^{-1}), stable suspensions of selenite (left) and satin spar (right) nanobelts. What was quite apparent from the appearance of the suspensions was that both liquids were white in hue. With regards to the potential utilization of the LPE method on Mars, a symbiotic relationship between the NASA dehydration studies is envisioned. The water created from the conversion of gypsum to anhydrite can in turn also be used to exfoliate the anhydrite. Potentially the process of making the nanobelts on Mars would then require very little payload contribution, saving on fuel and shipping costs. Additionally, to scale the LPE process to an appropriate level for use on Mars, more high throughput methodologies can be applied in place of sonication. Mainly those involving shear exfoliation,[21] or high-pressure homogenization,[22] which report production rates generally >5 g h^{-1} for layered materials.

SEM collages revealed morphological changes for selenite (Figure 1e) and satin spar (Figure 1f) during each processing step. As expected, structural differences due to their unique formation mechanisms were self-evident. However, both eventually descended into their basic nanobelt structure upon the completion of processing. For selenite, images of the as-received i) and ground bulk ii) mineral in Figure 1e presented a layered
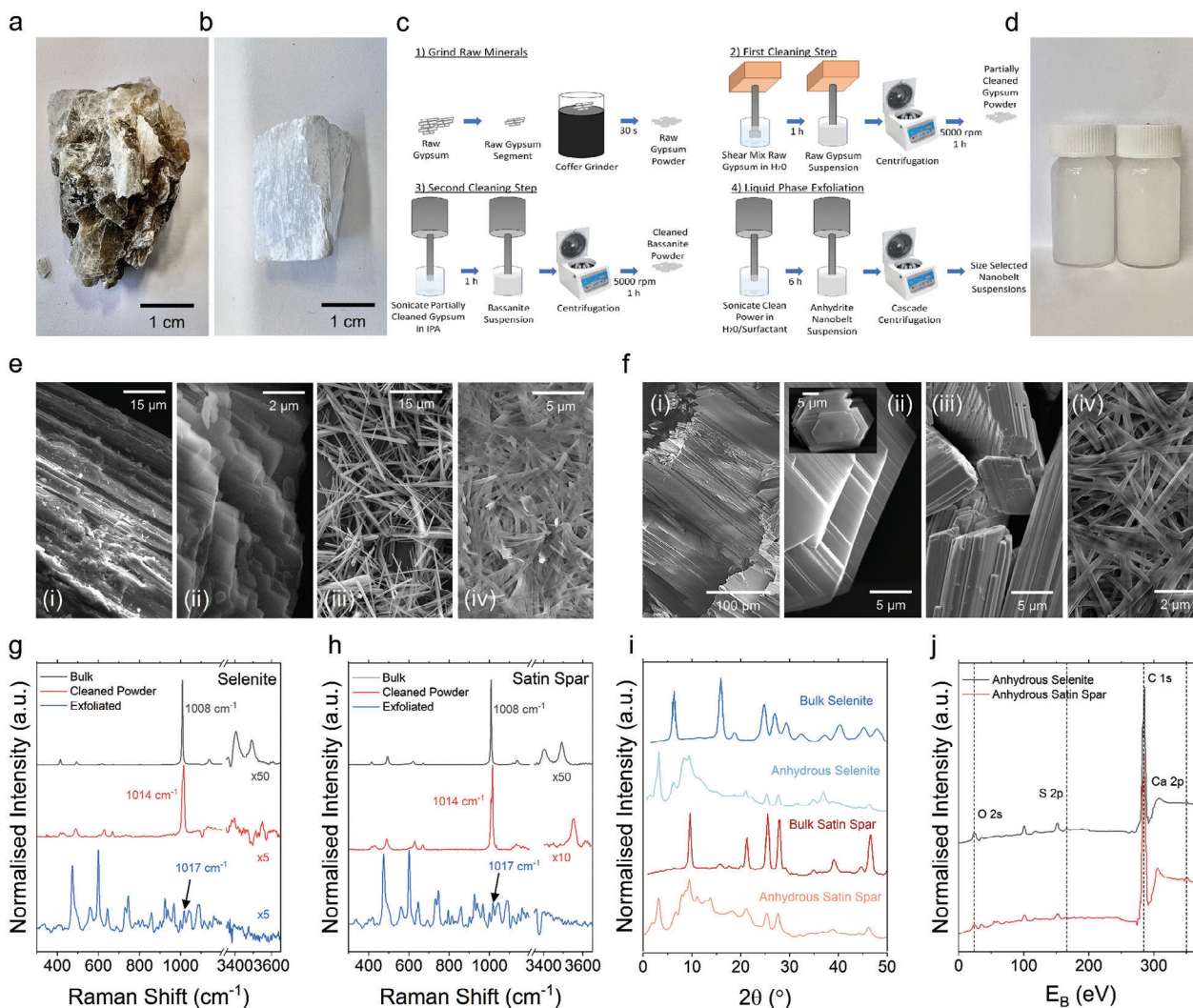
**ADVANCED
SCIENCE NEWS**

www.advancedsciencenews.com

**ADVANCED
FUNCTIONAL
MATERIALS**

www.afm-journal.de

Figure 1. Processing and Basic Characterization of Minerals. Optical photograph of the raw, bulk a) selenite and b) satin spar minerals. c) Graphical scheme depicting the procedural steps applied to process the raw minerals into a powder, which underwent a series of cleaning steps to yield bassanite powder that was liquid exfoliated to create anhydrous nanobelts. d) Optical photograph of an (left) anhydrous selenite and (right) anhydrous satin spar suspension. e,f) Scanning electron micrograph collage showing the various morphological stages of selenite and satin spar mineral during processing and exfoliation. Left to right: (i) as received bulk material, (ii) raw bulk powder, (iii) cleaned powder/bassanite powder, and a (iv) liquid exfoliated anhydrous nanobelt network. g,h) Raman spectra of selenite and satin spar samples during their various stages of crystal structure. i) X-ray powder diffraction spectra comparing the crystal structure change between the bulk powder and the nanobelts. j) X-ray photoelectron spectroscopy confirming the elemental composition of the nanobelt materials. Dashed lines denote peaks related specifically to oxygen, silicon, carbon, and calcium.

structure indicative of tabular crystal growth during formation. However, the clean processed powder of selenite iii) began to reveal the rigid nanobelt aggregates that make up the bulk structure. Through the LPE step iv), the delamination of the aggregates produced more flexible, individualized species. In contrast, in Figure 1f, satin spar presents a fibrous structure that remained in place for the as-received bulk i), powdered bulk ii), and cleaned processed powder iii). The only noticeable difference was the size of the crystals that made up the samples gradually decreased with each step. However, through the LPE step iv), individual nanobelts were confirmed to have been successfully delaminated from the fibrous crystals. The difference in exfoliation readiness between the two bulk materials, despite having a similar composition, can potentially be attributed to their unique

cleavage and hardness properties. With bulk satin spar having poorer cleavages (one difficult and two imperfect directions) and a higher hardness (3 Mohs) when compared to bulk selenite (perfect cleavage in one direction, distinct in two directions; hardness of 2 Mohs).[23]

2.2. Material Identification

Examining the materials via Raman spectroscopy, we note that for both selenite (Figure 1g) and satin spar (Figure 1h), significant shifting in the vibration $v1$ (a1) mode associated with SO_4^{2-} occurred.[24] Specifically, shifts in this characteristic gypsum mode at ≈ 1008 cm^{-1} appeared across the various stages of

mineral processing. Past studies have attributed $v1$ mode shifts with changes in the hydrous state and structural composition of calcium sulfate minerals.[25] In line with these previous reports, we note that for both sets of Raman spectra, the $v1$ mode in the bulk resided at the expected Raman shift of 1008 cm^{-1}. However, the mode moved to higher Raman shifts as both materials transitioned to the clean powder state (1014 cm^{-1}) and then to the exfoliated nanobelts (1017 cm^{-1}). Notably, the $v1$ mode also greatly decreased in intensity with each processing step. We report that these shifts in the $v1$ mode are indicative of the materials transitioning from a dihydrate state in the bulk (i.e., gypsum – $CaSO_4 \cdot 2H_2O$) to a hemihydrate state after undergoing cleaning (i.e., bassanite – $CaSO_4 \cdot \frac{1}{2}H_2O$) to their anhydrous form when they are exfoliated (i.e., anhydrite – $CaSO_4$).[25a] Additionally, the Raman shift position of the transitioning $v1$ mode for each processing step matched precisely the previously reported positions for each calcium sulfate phase.[25a,26] For all calcium sulfate minerals and their three phases, the two core constituents are sulfate tetrahedral (SO_4^{-2}) and calcium (Ca^{2+}) ions.[17] During the dehydration process to transition through the phases, the physical structure of the minerals undergoes large changes (see Figure S1, Supporting Information). Going from gypsum to bassanite, the alternating layers of water molecules and ions change to a mixed structure. Where Ca^{2+} ions now coordinate to SO_4^{-2} ions to compensate for the lack of charge balancing because of the decreased hydrogen bonding with water molecules.[14,17,27] This partial removal of water molecules results in the density of the structure increasing, as the spacing between ions decreases.[28] Further dehydration to anhydrite causes the formation of a structure devoid of water molecules, consisting of an ordered array of SO_4^{-2} ions, with alternating tetrahedral having Ca^{2+} ions coordinated to them.[17]
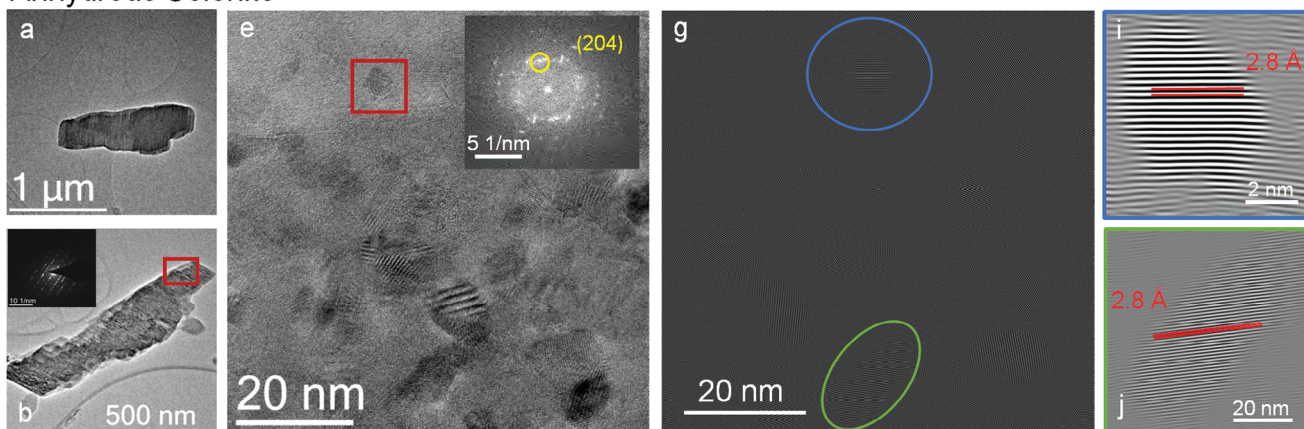
We further confirm the dehydration process by examining the Raman modes of water for each phase. For both bulk selenite and satin spar, water modes at 3404 and 3492 cm^{-1} were observed.[25a,26] As anticipated for bassanite minerals, or our clean powder, these modes moved to Raman shifts of 3554 and 3614 cm^{-1} respectively.[25a] Whereas, for the exfoliated nanobelts, or the anhydrous state, modes associated with water are expectedly absent.[25a,26] We note that even after two months (Figure S2, Supporting Information), anhydrite nanobelts do not convert back to bassanite or gypsum through ambient water absorption.[29] This implied that our procedure creates ultrastable, insoluble anhydrite.[30] Specifically with regards to the stability of anhydrite nanobelts on the Martian surface, the water vapor pressure on Mars is much larger than the equilibrium water vapor pressure required to induce rehydration of anhydrite to any of the hydrated phases.[29] This further strengthens the feasibility of the production and use of such nanomaterials by potential inhabitants. X-ray powder diffraction (XRD) spectra in Figure 1i also reflect the compositional changes seen previously via Raman. XRD showed large shifts in peak positions and the appearance of new peaks, confirming a structural change had occurred between the dihydrate bulk mineral and the anhydrous nanobelts.[31] Comparing the anhydrous nanobelts spectra for selenite and satin spar, we note that they are identical with regard to peak positions and shape. This is confirmation that though the appearance of the bulk materials differs, the basic building blocks of all calcium sulfate minerals are indeed similarly based

on SO_4^{-2} and Ca^{2+} ions structures. The only difference between phases is the level of hydration present. As noted above, this gives rise to the two mineral types presenting identical spectra during each processing step. One belief as to why such efficient dehydration is occurring during our processing is that bulk calcium sulfate minerals are in fact a mixed phase system, whereby only the external surface is dihydrate gypsum and the internal structure an anhydrous phase composed of nanobelts.[32] This is a plausible explanation for the abundance of anhydrous material generated by LPE. Through X-ray photoelectron spectroscopy (XPS) in Figure 1j, the chemical composition of the LPE nanobelts as expected remained similar to the bulk.[33] We note that peaks associated with Ca, S, and O appear in both selenite's and satin spar's anhydrous nanobelt spectra (fully annotated spectra can be found in Figures S3 and S4, Supporting Information, respectively). A strong C peak is also noted in both samples, which we attribute to the presence of residual surfactant and ambient organic matter absorbed during crystal formation. Essentially, our mineral processing procedure yields all hydrous forms in which calcium sulfate minerals can exist. Furthermore, it marks a dramatic improvement over energy-dense heating regimes,[25b] or time-intensive ball-milling processes[34] to bring about the dehydration of gypsum to yield its more commercially valuable bassanite or anhydrite forms.

2.3. Crystal Structure of Nanobelts

In **Figure 2**, we investigated the physical properties of the LPE anhydrite nanobelts through TEM. Here, typical low-resolution TEM micrographs of individual anhydrous selenite (Figure 2a,b) and satin spar (Figure 2c,d) nanobelts are shown. Noticeably in the micrographs, the elongated, belt-like shape of the materials, which aligns with SEM findings, is evident. However, the surface topography of the nanobelts was more apparent in TEM and appeared uneven, presenting a cross-hatch-like pattern. Nanobelts were composed of a lattice structure with planes perpendicular to the length, indicative of the natural growth mechanism of calcium sulfate structures.[35] Denoted by the red boxes in their respective figures (Figure 4b for selenite and Figure 4d for satin spar) select area electron diffraction (SAED) patterns for the anhydrous nanobelts (insets) were found to be similar to other calcium sulfate phases.[36] High-resolution transmission electron microscopy (HRTEM) on the nanobelts revealed both the surfaces of anhydrous selenite (Figure 2e) and satin spar (Figure 2f) to show the expected characteristic polycrystalline structure.[14] Whereby, the overall structure was comprised of bassanite nanoparticles embedded in the lattice. We identified the bassanite nanoparticles through SAED patterns (red boxes), where the expected (204) and (200) planes of bassanite are reported (respective figure insets).[37] Inverse Fast Fourier Transforms (IFFT) of the micrographs in Figures 2e,f with respect to the (204) plane (Figure 2g) and the (200) plane (Figure 2h), more clearly revealed the extent of the nanoparticle population. Examining the d-spacing of a select number of colour-coded nanoparticles, we confirmed their bassanite nature. We observed the characteristic bassanite lattice spacings of 2.8 Å (Figure 2i,j, red lines) and 6 Å (Figure 2k,l, red lines),[38] which corresponded to the (204) and (200) planes respectively. Essentially, though Raman

**ADVANCED
SCIENCE NEWS**

www.advancedsciencenews.com

**ADVANCED
FUNCTIONAL
MATERIALS**

www.afm-journal.de

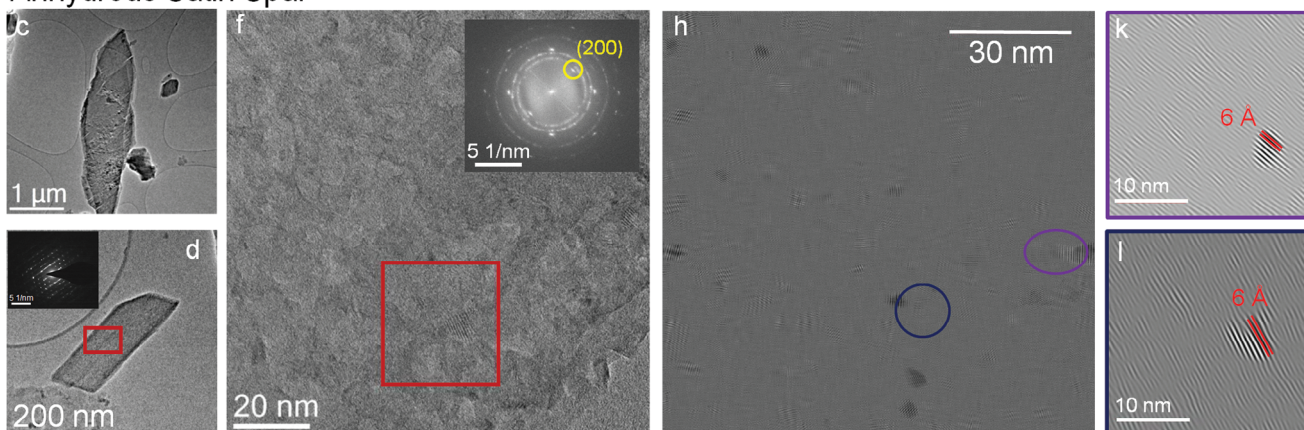## Anhydrous Selenite

Anhydrous Satin Spar

Figure 2. Nanobelt mesocrystal structure. a–d) Low resolution transmission electron micrographs of anhydrous selenite and satin spar nanobelts. Red boxes in figures b and d denote the regions in which the respective inset select area electron diffraction patterns were taken. e,f) High resolution transmission electron micrographs showing the lattice composition of the anhydrous selenite and satin spar nanobelts, respectively. Red box in figure (e,f) represents the region in which the select area electron diffraction patterns of bassanite nanoparticles were taken, presenting typical Miller (hkl) indices of (204) and (200) respectively. g,h) Inverse Fast Fourier Transform of figures e and f with respect to the (204) and (200) planes of the bassanite nanoparticles, respectively. A select number of nanoparticles are highlighted by color-coded rings. i–l) The characteristic d-spacing (red lines) for the (204) and (200) planes of bassanite were found for the respective color highlighted nanoparticles.

shows the overall structure of the nanobelts to be anhydrite, the presence of bassanite nanoparticles in TEM suggests that anhydrites may not undergo a full dehydration conversion. As bassanite is believed to be a nucleation point for calcium sulfate phase transitions, the noted sparsity of the bassanite nanoparticle may contribute to the long term stability of insoluble anhydrites.[30]

2.4. Size Selection and Statistical Analysis of Individual Nanobelts

Uniquely, with the nanobelts suspended in liquid, it lends toward the application of centrifugation techniques to separate colloids into size fractions of decreasing dimensions.[39] Through this technique, valuable information with regard to size-dependent nanobelt attributes can be empirically derived.[40] This particular mode of liquid sample size selection is a method ap-

plied already in the International Space Station in a zero-gravity environment.[41] Combined with the low relative centrifugal force (RCF) required to size-select our anhydrous nanobelts, the use of centrifugation lends well to its application on Mars and its lower planetary gravity. In **Figure 3**, a collage of atomic force microscopy (AFM) images shows anhydrous selenite (top) and satin spar (bottom) nanobelt samples that have been drop-casted onto a silicon substrate as a function of RCF. Noted for both sample sets, as RCF value increased from 0.12 to 0.48 g, the apparent length and height profiles of the nanobelts began to decrease. This is a common occurrence noted previously for other nanobelt systems[42] and nanosheets.[43] In **Figure 4**, we quantitatively assess the dimensions of the nanobelts for different RCF value samples through statistical AFM. For the nanobelts, we described their shape in terms of their longest dimension (length, L), the L's perpendicular bisector (width, W), and the profile height of the nanobelt at the L's midpoint (thickness, t). AFM histograms of
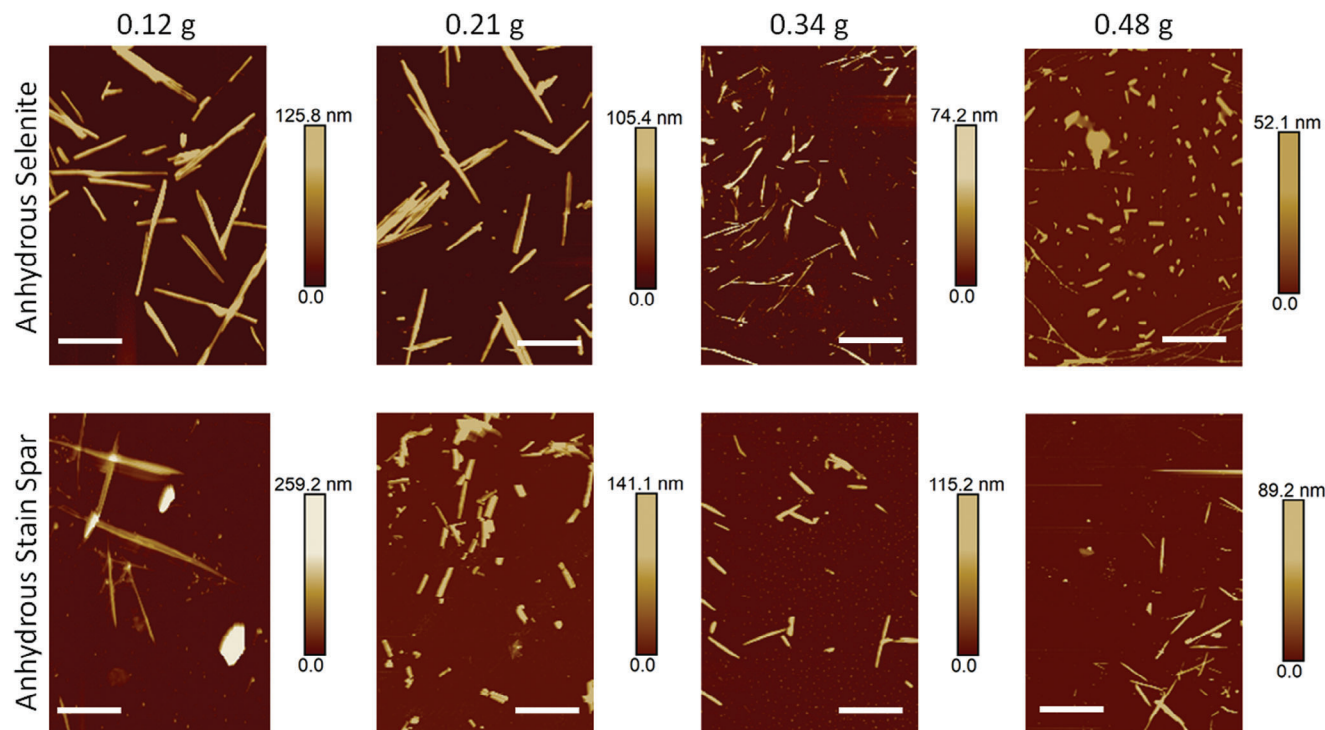
Figure 3. Size selected nanobelts. Representative atomic force microscopy images of drop casted nanobelt suspensions on silicon wafers as a function of relative centrifugal force (RCF = 0.12, 0.21, 0.34, 0.48 g). Both anhydrous (top row) selenite and (bottom row) satin spar presented suspensions that had nanobelt dimensions that decreased as a function of increasing RCF. Scale bars equal to 6000 nm.

L (Figure 4a,b), W (Figure 4c,d), and t (Figure 4e,f) of anhydrous selenite and satin spar showed that each dimension progressively decreased with RCF. For anhydrous selenite in Figure 4g, mean length ($<L>$) decreased from 5480 ± 195 nm for an RCF = 0.12 g to 1096 ± 32 nm at RCF = 0.48 g. Similarly, over the same RCF range, mean width ($<W>$) and mean thickness ($<t>$) decreased from 320 ± 6 to 107 ± 3 nm and 149 ± 3 to 48 ± 1 nm, respectively. As a function of t in the same figure, L and W were observed to follow individual power-law scalings with exponents of 2 and 1, respectively. In Figure 4h, a similar behavior in nanobelt dimensions was seen for anhydrous satin spar, with $<L>$ and $<W>$ decreasing from 4482 ± 132 to 1278 ± 51 nm and 363 ± 8 to 197 ± 5 nm, respectively. Furthermore, $<t>$ decreased from 116 ± 3 to 45 ± 1 nm, which we note to be the same value range observed for the selenite-based nanobelts. This implies that during LPE, nanobelts are more prone to scission rather than debundling. This is also reflective of the mesocrystal planes of the nanobelts appearing to being perpendicular to L in TEM micrographs in Figure 2. However, as a function of t, L, and W in Figure 4h scaled according to unique power-law scalings with exponents of 1.4 and 0.8, respectively. Plotting anhydrous selenite aspect ratio (L/t) as a function of t in Figure 4i, values proportionally scaled with t from 58 ± 3 to 27 ± 1 as RCF values increased from 0.12 to 0.48 g. For the anhydrous satin spar in Figure 4j, L/t decreased from 44 ± 2 to 26 ± 2 over a similar RCF value range according to a $t^{0.7}$ scaling. We report that the aspect ratio of the nanobelts was on par with LPE nanosheets (typically <100)[44] but smaller than carbon nanotubes that were debundled in the liquid phase (typically >250).[45]

2.5. Optical and Electronic Properties of Nanobelts

Through UV–vis spectroscopy (UV–vis), the light absorption properties of the anhydrous selenite (**Figure 5a**) and satin spar (Figure 5b) nanobelt suspensions were examined via normalized extinction spectra as a function of RCF value. For both materials, the threshold for absorption shifted to smaller wavelengths as RCF values increased. Through AFM analysis, these spectral shifts can also be interpreted as absorption properties decreasing with nanobelt dimension. As bulk gypsum is reported to be a wide E_g insulator, these findings imply that unexpected electronic transitions were occurring for the exfoliated nanobelts. In Figures 5c,d, UV–vis spectra were converted to Tauc plots to extrapolate information about the optical E_g of each nanobelt species as a function of RCF. Though extinction spectra are comprised of components associated with absorption and scattering effects,[46] Tauc plots from extinction spectra still provide accurate predictions of E_g for large aspect ratio rod-like[47] and disk-like[48] nanomaterials. In Figure 5c, E_g for anhydrous selenite was observed to increase from ≈2.24 to ≈3.93 eV as RCF values rose from 0.12 to 0.48 g. While for the anhydrous satin spar in Figure 5d, E_g increased from ≈2.67 to ≈3.86 eV for the same RCF range. Both minimum E_g values here are far below the expected bulk value of >5 eV.[49] Previous reports on the delamination of other mineral types showed that the initial transition from insulating to semiconducting behavior was due to lattice relaxation.[50] For LPE phyllosilicate mineral nanosheets,[7] this manifested as XPS peak shifts and XRD peak narrowing. However, these findings do not appear to hold true for gypsum, as no
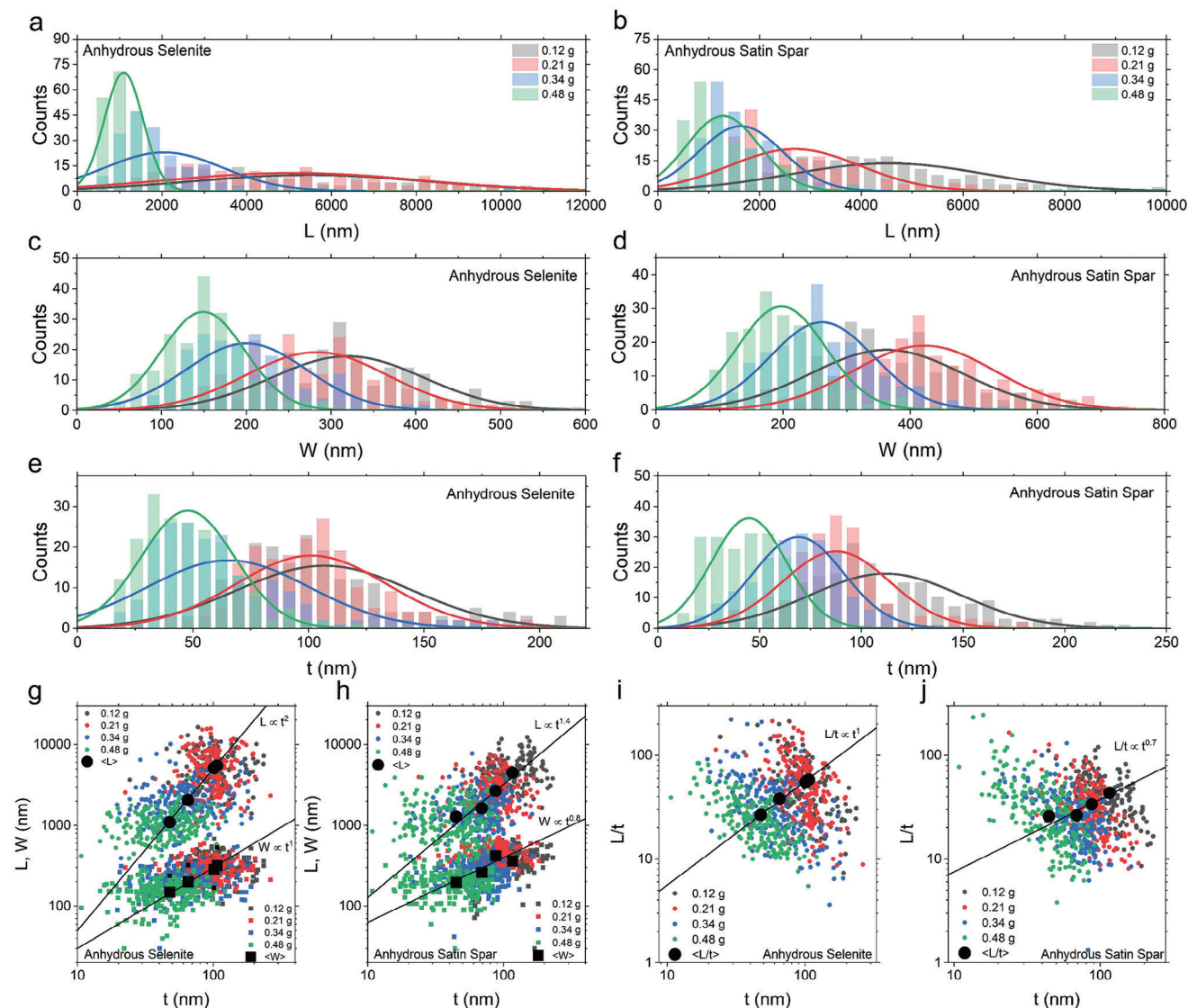
**ADVANCED
SCIENCE NEWS**

www.advancedsciencenews.com

**ADVANCED
FUNCTIONAL
MATERIALS**

www.afm-journal.de

Figure 4. AFM analysis of size selected nanobelt suspensions. a–f) Histograms showing statistical atomic force microscopy (AFM) analysis associated with the length (L), width (W) and, thickness (t) of anhydrite nanobelts as a function of relative centrifugal force (RCF). g,h) Length and width of selenite and satin spar anhydrite nanobelts for a range of RCF values as a function of thickness followed individual power-law like scalings (solid lines). i,j) Aspect ratio (L/t) for both anhydrous selenite and satin spar nanobelts also scaled according to unique power-laws (solid lines). With selenite L/t scaling proportionally with nanobelt thickness (i.e., exponent of 1) and satin spar L/t scaled with an exponent of 0.7 as a function of t. For each nanobelt dimension (i.e., L, W, t), the sample size was 200 individual measurements.

consistent data shifts were observed. This is likely due to a complexity of mechanisms associated with transitioning from bulk gypsum to anhydrite nanobelts. However, it has been reported that high levels of residual stress can be found in gypsum and its derivatives due to the natural crystal formation process,[31b,51] and the presence of contaminates.[52] Essentially, strain relaxation during delamination could plausibly still be the root cause of the initial E_g drop. Nonetheless, strain relaxation does not account for the total occurrence of E_g tunability. When plotting E_g versus $\langle t \rangle$ and $\langle W \rangle$ in Figure 5e, values for E_g were seen to scale with an exponent of −2 for both data sets in accordance with quantum confinement.[53] Similarly, phyllosilicate nanosheet E_g was also observed to follow an analogous scaling.[7]

2.6. Applications

Previously, semiconducting nanomaterials like transition metal dichalcogenides have shown great promise as optoelectronic devices.[54] With the unexpected semiconducting properties of the nanobelts here, we examined the photoresponse of spray-printed networks of anhydrous satin spar on a glass substrate (Figure S5, Supporting Information). Due to their large lateral size, the nanobelts making up the printed network were visible via an optical microscope in **Figure** 6a. For the figure's inset, the long rod-like shape of the nanobelts was self-evident. In Figure 6b, current-voltage (I--V) curves associated with the network were investigated under dark and illuminated

ADVANCED
SCIENCE NEWS

www.advancedsciencenews.com
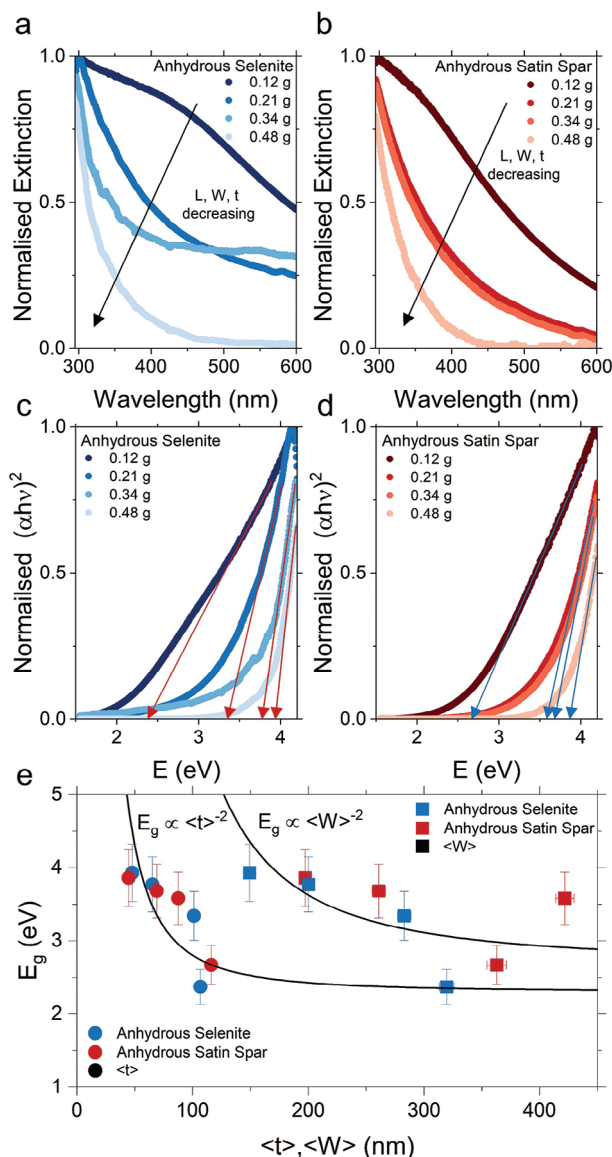
ADVANCED
FUNCTIONAL
MATERIALS

www.afm-journal.de

Figure 5. Size dependent optical and electrical properties. a,b) Normalized UV–vis extinction spectra of anhydrous selenite and satin spar, respectively, as a function of relative centrifugal force (RCF). As a resultant, spectral lines are noted to scale with decreasing length (*L*), width (*W*), and thickness (*t*) associated with the size selected nanobelt suspensions previously measure via AFM. c,d) Tauc plots derived from the UV-Vis data in figure a and b allow for the calculation of the optical bandgap (E_g) for anhydrous selenite and anhydrous satin spar. The values of E_g for both materials were seen to incrementally increase with RCF value, and thus decreasing nanobelt dimensions. Specifically, E_g scaled with both anhydrite nanobelt mean thickness ($<t>$) and mean width ($<W>$) according to quantum confinement effects, defined by $<t>^{-2}$ and $<W>^{-2}$ scalings (solid lines).

conditions for a range of monochromatic light sources (650, 532, and 380 nm). It was observed that for *I–V* curves under dark conditions, or excitation wavelengths with energies below the nanobelt E_g of ≈2.6 eV, all curves had similar slopes over a ±5 V range. Furthermore, these curves presented a near linear trend indicative of a resistive element. However, when light with

a wavelength of 380 nm (≈3.3 eV) illuminated the network, the open circuit voltage (V_{OC}) shifted from −1.231 V to 0.276 V. In the forward-bias region, the change in V_{OC} resulted in a crossover voltage of ≈2 V between the 380 nm illumination and the other curves. Most noticeably the shape of the 380 nm curve in this region appeared as that of a diode, with a knee point beginning to appear at ≈3.3 V and the current showing saturation. Furthermore, the slope in the reverse bias drastically increased, making anhydrous satin spar nanobelts potentially interesting for photosensitive Zener diodes.

Owing to their exciting electronic properties and rough amorphous surfaces that are fit for reaction nucleation, the potential for hydrogen propagation of anhydrite nanobelts was examined. Electrochemical electrodes were formed by filtering nanobelt suspensions of anhydrous selenite and satin spar onto a membrane, after which they were transferred onto glassy carbon (GC). Polarization curves in Figure 6c for the two nanobelt electrodes presented onset potentials (V_{onset}) of 293 ± 21 mV versus RHE and 302 ± 16 mV versus RHE, respectively. While the bare GC electrode had a value of 407 ± 27 mV versus RHE. Through Tafel plots in Figure 6d, the Tafel slope (*S*) values were extrapolated. Anhydrous selenite presented a value of $S = 94 ± 7$ mV dec^{-1}, anhydrous satin spar a value of $S = 117 ± 31$ mV dec^{-1} and bare GC a much larger slope of $S = 165 ± 19$ mV dec^{-1}. Furthermore, derived exchange current density (J_0) values for each electrode were 0.0019 ± 0.0002 mA cm^{-2}, 0.0014 ± 0.0006 mA cm^{-2} and 0.0011 ± 0.0002 mA cm^{-2}, respectively. Comparatively, LPE biotite micene mineral electrodes of similar thickness and density were reported to present a set of metric values of V_{onset} ≈ 234 mV, S ≈ 95 mV dec^{-1} and J_0 ≈0.0035 mA cm^{-2}.[7] In general, we found anhydrite nanobelts to be quite competitive when compared to other nanomaterial types. The nanobelts here greatly surpassed most other nanomaterial catalytic performances, which can be defined as having both low V_{onset} and *T* values (Figure S6 and Table S1, Supporting Information). Due to its natural abundance, anhydrous selenite nanobelts in particular prove to be a potential cost-effective replacement for more widely utilized, less sustainably produced active materials. The demonstration of HER via these materials is of such importance as it is a mode in which clean fuel can be created and applied on Mars using only Martian-based materials. As previously mentioned, water can be created from the dehydration of gypsum, which yields anhydrite. Additionally, sulfuric acid, used here in this study as an electrolyte, can also be procured through reacting materials also found on Mars.[55] Most vital is the potential to leave our reliance on fossil fuels behind on Earth as we as humans branch out.

To take advantage of the large intrinsic stiffnesses associated with single-crystal gypsum,[56] mixed-phase anhydrous selenite nanobelt/polyvinyl alcohol (ASN/PVA) nanocomposite materials were made. By creating a range of ASN/PVA nanocomposites with various volume fractions (V_f) of filler material, the mechanical reinforcement properties of anhydrous selenite nanobelts were investigated. In Figure 6e, an optical photograph of a typical V_f ≈ 0.2% ASN/PVA sample was shown to be uniform and highly transparent. Through representative stress–strain curves in Figure 6f, variations in the nanocomposite properties as a function of filler loadings were observed. These changes manifested themselves in Figure 6g as a linear scaling in Young's modulus (*Y*), from ≈34 kPa at V_f ≈ 0% up to 44 kPa at a critical
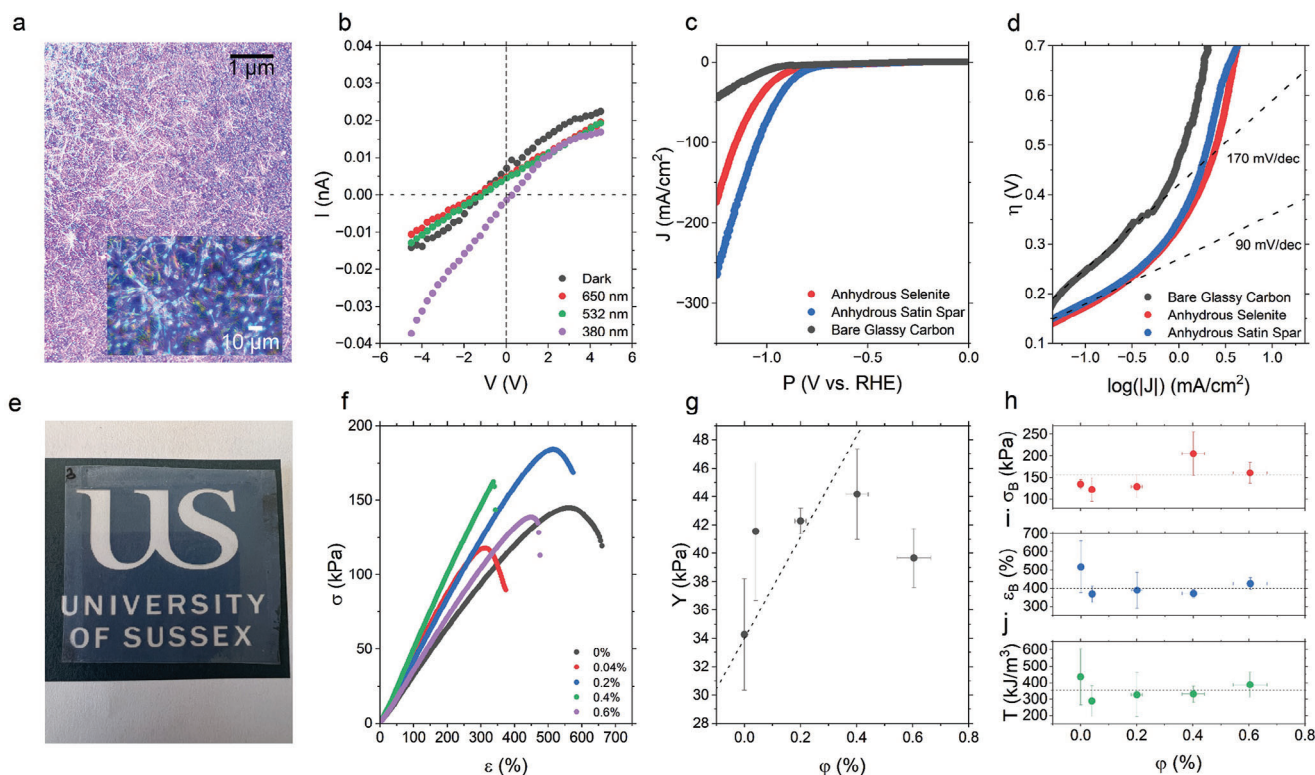
Figure 6. Applications of nanomineral nanobelts. a) Optical micrographic image of a 2 µm thick anhydrous satin spar nanobelt network spray printed onto a glass substrate. Inset is a zoomed in look at the network. b) Current verse voltage curves of the anhydrous satin spar nanobelt network from figure a in the dark and as a function of various illumination wavelengths. c) Polarization curves for anhydrite nanobelts and the bare glass carbon electrode, with their corresponding d) Tafel plots. Dashed lines in figure d denote the Tafel slope. e) Optical image of 0.2 vol% anhydrous satin spar/PVA nanocomposite on top of the University of Sussex logo. f) Representative stress-strain curves of PVA nanocomposites as a function of anhydrous satin spar loading level. g–j) Extrapolated mechanical metrics Young's modulus (Y), stress at break (σ_B), strain at break (ϵ_B) and toughness (T) as a function of loading level. Dashed line in figure g is a fit of Equation (1) and dashed lines in figures are mean values of 155 kPa, 400% and 350 kJ m^{-3} respectively.

loading of $V_f \approx 0.4\%$. After which, values decreased to ≈40 kPa at 0.6 vol% due to filler aggregation.[57] We note that our 1.3 fold increase in modulus at 0.4 vol% was on par with the reinforcement of PVA by graphene oxide (1.5 fold increase at 0.24 vol%),[58] graphene (1.6 fold increase at 0.36 vol%),[59] boron nitride (1.3 fold increase at 0.11 vol%),[60] and molybdenum disulfide (1.1 fold increase)[61] fillers. One other key advantage, unlike the other nanofillers listed above, anhydrous selenite did not affect the opaqueness of the nanocomposites. Using the rule of mixtures and the assumption that the nanobelts are in plane,[62] an estimation of anhydrous selenite (Y_{AS}) and composite (Y_C) moduli can be made through the expression,

$$Y_C = Y_{AS} V_f + Y_P \left(1 - V_f\right) \tag{1}$$

where Y_P is the polymer modulus. Fitting Equation (1) in Figure 6g to the low V_f regime, good agreement was found with the data, and a Y_{AS} value of 3.6 MPa extrapolated. We note that the Y_{AS} value is far below the potential single crystal theoretical value of ≈40 GPa,[56a] however this is unsurprising when considering that other mechanical properties remained invariant with V_f. In Figures 6h–j, stress at break (σ_B), strain at break (ϵ_B), and toughness (T) are scattered around mean values of 155 kPa, 400%, and 350 kJ m^{-3} respectively. This would suggest that the mechanism

for failure in ASN/PVA nanocomposites was the filler/polymer interface.[63] In fact, we find that our evaluation of Y_{AS} was consistent with the shearing of gypsum crystallites.[64] Essentially, stress transfer to the fillers from the polymer matrix results in smaller crystallites being stripped from the nanobelts, causing the interface to fail, rather than the nanobelts fracturing. This is unsurprising when considering the mesocrystal morphology of the nanobelts seen in TEM, where the surfaces are comprised of aggregates rather than a single crystal.[65]

3. Discussion

In conclusion, we demonstrate that naturally occurring bulk terrestrial gypsum can be sustainably processed to produce a wide range of commercially valuable minerals based on its different hydrous phases. Through simple liquid processing techniques, gypsum, bassanite, and anhydrite materials can be easily produced. We specifically investigated the properties of anhydrite via liquid exfoliation methods to create water-based suspensions that contained nanobelts that we characterized through a variety of spectral and microscopy techniques. Through these findings, anhydrite nanobelts were discovered to have tunable electronic properties down to semiconducting behaviors that were controlled by the nanobelt's dimensions. With their broad range

**ADVANCED
SCIENCE NEWS**

www.advancedsciencenews.com

**ADVANCED
FUNCTIONAL
MATERIALS**

www.afm-journal.de

of superlative properties, nanobelts based on anhydrous selenite and satin spar were demonstrated as effective optoelectronic devices, electrochemical electrodes, and fillers for the mechanical reinforcement of textiles. Our simple methodology and findings lay the foundation to potentially support future exploration and inhabitation of Mars through the usage of its abundant gypsum mineral deposits.

4. Experimental Section

Materials: Bulk gypsum crystals were purchased from Geology Superstore. Selenite (Morocco) and Satin spar (Turkey) were procured as 2-inch × 2-inch samples.

Gypsum Processing Procedure: A mass of 2 g was removed from the bulk gypsum crystals and powdered using a UUOUU 200 W Bowl Spice Grinder. A 20 mg mL^{-1} raw bulk powder/deionized water solution was made up and then shear mixed at room temperature for 1 h at 5000 rpm. After shearing, the mixture was then centrifuged at 5000 rpm. The supernatant was discarded, and the sediment was redispersed in IPA at 20 mg mL^{-1}, first by mechanical shaking in hand. The IPA solution was then ultrasonicated (Sonics Vibra-cell VCX130, flathead probe) at 5 °C for 1 h at 60% amplitude with a 6 s on 2 s off configuration. The mixture was then centrifuged at 5000 rpm, with the supernatant again discarded and the bassanite sediment kept. The clean powdered bassanite was then stored in an oven at 60 °C overnight.

Liquid Phase Exfoliation: Clean powdered bassanite was added to a sodium cholate solution (Sigma–Aldrich BioXtra, ≥99%, 6 mg mL^{-1}) at 2 mg mL^{-1} and ultrasonicated (Sonics Vibra-cell VCX130, flathead probe) at 5 °C for 5 h at 60% amplitude with a 6 s on 2 s off configuration. The resultant anhydrous nanobelt suspensions were then cascade centrifuged[39a] at RCF values of 0.12, 0.21, 0.34, and 0.48 g.

Scanning Electron Microscopy: Samples were drop casted onto a silicon wafer. For the LPE samples a RCF = 0.12 g sample was used for both selenite and satin spar. The wafer was then attached to an SEM stub using a carbon tab and silver paint. All samples were gold coated with a ≈5 nm layer. The topography of the samples were examined using a Inspect F from FEI Company (Netherlands) in SE2 mode.

Raman Spectroscopy: Suspensions of raw gypsum powder, bassanite powder and anhydrous nanobelts (RCF = 0.12 g) were drop casted onto a glass slide. A Renishaw in via confocal Raman microscope with 0.8 cm^{-1} spectral resolution and 532 nm laser (type: solid state, model: RL53250) was used for measurements. A 2400 mm^{-1} grating in 100× magnification and 5 mW laser power was used. For each sample curve, an average of ten spectra was used.

X-Ray Powder Diffraction: Powdered bulk and nanobelt suspensions (RCF = 0.12 g) were filtered onto nitrocellulose membranes (25 nm pore size). For the nanobelt sample membranes, they were washed with 1 L of deionized water to remove residual surfactant. All membranes after filtering were then left in the oven at 60 °C overnight to dry. A spatula was then used to scrape filter material for the membranes, with the resultant powder collected in a plastic capillary tube. The data was generated on a Rigaku Gemini Ultra using the powder mode in the CrysAlisPro (version 171.42.75) software. The data was collected using Cu radiation (1.5418A) over a range of 125 degrees in 2theta.

X-Ray Photoelectron Spectroscopy: Nanobelt suspensions (RCF = 0.12 g) were filtered onto nitrocellulose membranes (25 nm pore size) and washed with 1 L of deionized water to remove residual surfactant. The membranes were then left in the oven at 60 °C overnight to dry. The membranes were measured using a Kratos Axis SUPRA spectrometer utilizing a monochromatic Al Kα (1486.6 eV) X-ray source. Survey spectra had an energy step of 1 and 160 eV analyzer pass energy. The spectra were analyzed using CASA XPS software. Shirley baselines were used to subtract the background for quantification purpose. The spectra were calibrated using the B.E. of the C 1s peak at 284.5 eV due to the use of the charge neutralizer during the spectra acquisition.

Transmission Electron Microscopy: RCF = 0.12 g anhydrous nanobelt suspensions were drop-casted on a 300-mesh carbon coated copper grids and dried. TEM measurements were performed in an image corrected FEI (Thermo Fisher) Titan Cube having a spherical aberration corrector at the objective lens and operating at 300 kV. Electron dose was optimized to reduce any beam induced damage of the samples during the measurements.

Atomic Force Microscopy: Suspensions were drop casted onto a heated silicon wafer (≈70 °C). After which, the wafers were washed with deionized water to remove residual surfactant. A Dimension icon Bruker positioned in an insulated box over an anti-vibrant stage to minimize environmental noise and building vibrations was used for measurements. For all measurements, a ScanAsyst Air tip probe with a spring constant of 0.4 N m^{-1}, and a tip–sample contact force of 5.0 nN was used. To obtain a good statistical average for length, width and thickness; 200 measurements for each dimension was performed through line profile analysis of individual nanobelts.

UV–Vis Spectroscopy: Measurements were performed using a Shimadzu UV-3600 Plus spectrophotometer from 200 to 800 nm using a quartz cuvette (path length, 1 cm). Sample curves were an average of five spectra.

Printed Anhydrous Satin Spar Nanobelts: A KMOON airbrush stylist (nozzle diameter = 0.2 mm, fluid cup capacity = 9 cc) was used at a pressure of 3.6 bar to deposit a 1.2 mg mL^{-1} suspension of anhydrous satin spar nanobelts onto a glass substrate. Optical images of the network were taken using an Olympus BX53M with 4K digital CCD camera. The thickness of the sample was measured using a Bruker DektakXT profilometry. The uniform 25 mm × 25 mm nanobelt network had silver contacts painted (length 25 mm) onto the central surface of the network at an electrode distance of 3 mm. A Keithley 2614B voltage source using the voltage range of −5–5 V. For all measurements, the sample was covered by a blackened tarp. Lights sources (5 mW laser pen) were positioned ≈10 cm away from the sprayed network surface. Standard error for all source wavelengths was ±10 nm.

Electrochemical Analysis: Suspensions (RCF = 0.12 g) of known concentration found via vacuum filtration, were filtered onto nitrocellulose membranes (25 nm pore size) and washed with 1 L of deionised water to remove residual surfactant. Nanobelt networks (density = 0.2 mg cm^{-2} ± 0.013, thickness = 410 nm ± 150 nm) on the membrane were then cut into pieces and transferred onto glassy carbon rods (3 mm diameter, BASi) by placing the membrane (network side down) on the substrate. The membrane was then wetted with isopropanol and pressure applied. Acetone vapor and acetone baths were used to then dissolve the membrane, leaving the bare network on the substrate. Linear sweep voltammetry and electrochemical impedance spectroscopy were performed using a Gamry Reference 3000 potentiostat in a three-electrode configuration. The glassy carbon electrode was used as the working electrode, while a platinum wire and Ag/AgCl (3 M KCl) was used as the counter and the reference electrode, respectively. Linear sweep voltammetry experiments were performed with a scan rate of 5 mV s^{-1} from 0 V to −1.5 V (vs RHE) in 0.5 M H_2SO_4 to investigate the hydrogen evolution performance. The measured potential was converted to the RHE scale by adding +0.2 V, measured with respect to a Gaskatel Hydroflex H_2 reference electrode.

Anhydrous Selenite Nanobelt Nanocomposites: A 20 mg mL^{-1} stock solution of PVA (Sigma–Aldrich, product code: 102 415 238, CAS-No: 9002-89-5, average M_w between 30000 and 70000) was created by mixing PVA powder in deionized water at 180 °C at 700 rpm for 1 h. To make nanocomposites with different mass fractions of filler, various volumes of anhydrous selenite (6 mg mL^{-1}) were mixed into a volume of PVA solution, with all samples having a constant total volume of 20 mL. The mixed phase solutions were then mixed at 180 °C at 700 rpm for 1 h. After which, the solution was left to cool ambiently for a few minutes and then poured into a petri dish. The petri dish was then placed in a vacuum oven at 60 °C under a vacuum of 900 mbar. Nanocomposite filler volume fraction was calculated from the mass fraction using the densities of the polymer (1190 kg m^{-3}) and the filler (2960 kg m^{-3}). Nanocomposites were cut into 47 mm × 5 mm segments and analyzed using a Stable Micro Systems TA-TXplus at a test speed of 0.6 mm^{-1}s. Thickness of each test segment was measure using a screw gauge.

**ADVANCED
SCIENCE NEWS**

www.advancedsciencenews.com

**ADVANCED
FUNCTIONAL
MATERIALS**

www.afm-journal.de

Supporting Information

Supporting Information is available from the Wiley Online Library or from the author.

Conflict of Interest

The authors declare no conflict of interest.

Author Contributions

C.S.B. conceived and designed experiments. C.W. created all samples for the study. C.W., A.J., A.K.A.A., Y.H., and S.M.R. performed experiments. C.S.B. analyzed and modeled data. D.G.P., S.M.R., R.A., and C.S.B. contributed materials, tools, and supervision. C.S.B wrote and revised the paper.

Dedications

For O.R.B. – You always make each day a special day, by just being you.

Data Availability Statement

The data that support the findings of this study are available from the corresponding author upon reasonable request.

[1] a) M. F. L. De Volder, S. H. Tawfick, R. H. Baughman, A. J. Hart, *Science* **2013**, *339*, 535; b) S. Rathinavel, K. Priyadharshini, D. Panda, *Mater. Sci. Eng., B* **2021**, *268*, 115095.

[2] a) R. Yan, D. Gargas, P. Yang, *Nat. Photonics* **2009**, *3*, 569; b) C. Jia, Z. Lin, Y. Huang, X. Duan, *Chem. Rev.* **2019**, *119*, 9074.

[3] a) A. G. Kelly, D. O'suilleabhain, C. Gabbett, J. N. Coleman, *Nat. Rev. Mater.* **2022**, *7*, 217; b) H. Kaur, J. N. Coleman, *Adv. Mater.* **2022**, *34*, 2202164.

[4] a) A. K. A. Aljarid, M. Dong, Y. Hu, C. Wei, J. P. Salvage, D. G. Papageorgiou, C. S. Boland, *Adv. Funct. Mater.* **2023**, *33*, 2303837; b) A. A. K. Aljarid, K. L. Doty, C. Wei, J. P. Salvage, C. S. Boland, *ACS Sustain. Chem. Eng.* **2023**, *11*, 1820.

[5] a) S.-H. Park, P. J. King, R. Tian, C. S. Boland, J. Coelho, C. Zhang, P. Mcbean, N. Mcevoy, M. P. Kremer, D. Daly, J. N. Coleman, V. Nicolosi, *Nat. Energy* **2019**, *4*, 560; b) C. Zhang, S.-H. Park, A. Seral-Ascaso, S. Barwich, N. Mcevoy, C. S. Boland, J. N. Coleman, Y. Gogotsi, V. Nicolosi, *Nat. Commun.* **2019**, *10*, 849.

[6] a) Y. Cui, Z. Zhou, T. Li, K. Wang, J. Li, Z. Wei, *Adv. Funct. Mater.* **2019**, *29*, 1900040; b) C. Ma, Y.-F. Liu, Y.-G. Bi, X.-L. Zhang, D. Yin, J. Feng, H.-B. Sun, *Nanoscale* **2021**, *13*, 12423.

[7] C. Wei, A. Roy, M. Tripathi, A. K. A. Aljarid, J. P. Salvage, S. M. Roe, R. Arenal, C. S. Boland, *Adv. Mater.* **2023**, *35*, 2303570.

[8] J. K. Warren, *Evaporites:Sediments, Resources and Hydrocarbons*, Springer Science & Business Media, Luxembourg **2006**.

[9] Gypsum mine production top countries 2022, Statista Research Department, **2023**. Weblink: https://www.statista.com/statistics/264936/global-gypsum-production-by-major-countries/.

[10] *Gypsum Market Outlook 2023 to 2033* Future Market Insights, **2023**.https://www.futuremarketinsights.com/reports/gypsum-market.

[11] J. J. Wray, S. W. Squyres, L. H. Roach, J. L. Bishop, J. F. Mustard, E. Z. Noe Dobrea, *Icarus* **2010**, *209*, 416.

[12] E. L. Scheller, B. L. Ehlmann, R. Hu, D. J. Adams, Y. L. Yung, *Science* **2021**, *372*, 56.

[13] a) P. J. van Susante, J. Allen, T. C. Eisele, E. F. Medici, K. Zacny, in *2018 AIAA SPACE and Astronautics Forum and Exposition*, American Institute of Aeronautics and Astronautics, Reston, Virginia **2018**; b) P. J. van Susante, J. S. T. Allen, T. C. Eisele, E. F. Medici, M. S. Foetisch, K. A. Zacny, Z. Fitzgerald, Water Extraction from Rock Gypsum on Mars. *Earth and Space* **2021**, 653.

[14] A. E. S. Van Driessche, L. G. Benning, J. D. Rodriguez-Blanco, M. Ossorio, P. Bots, J. M. García-Ruiz, *Science* **2012**, *336*, 69.

[15] a) T. M. Stawski, A. E. S. Van Driessche, M. Ossorio, J. Diego Rodriguez-Blanco, R. Besselink, L. G. Benning, *Nat. Commun.* **2016**, *7*, 11177; b) C. Jia, G. Zhu, B. A. Legg, B. Guan, J. J. De Yoreo, *Cryst. Growth Des.* **2022**, *22*, 6582.

[16] M. Bąbel, *Acta Geol. Pol.* **2004**, *54*, 219.

[17] A. E. S. Van Driessche, T. M. Stawski, L. G. Benning, M. Kellermeier, in *New Perspectives on Mineral Nucleation and Growth*, (Eds: A. E. S. Van Driessche, M. Kellermeier, L. G. Benning, D. Gebauer), Springer International Publishing, Cham **2017**.

[18] A. A. Jafarzadeh, C. P. Burnham, *Eur. J.Soil Sci.* **1992**, *43*, 409.

[19] C. Capello, U. Fischer, K. Hungerbühler, *Green Chem.* **2007**, *9*, 927.

[20] V. Nicolosi, M. Chhowalla, M. G. Kanatzidis, M. S. Strano, J. N. Coleman, *Science* **2013**, *340*, 1226419.

[21] K. R. Paton, E. Varrla, C. Backes, R. J. Smith, U. Khan, A. O'neill, C. Boland, M. Lotya, O. M. Istrate, P. King, T. Higgins, S. Barwich, P. May, P. Puczkarski, I. Ahmed, M. Moebius, H. Pettersson, E. Long, J. Coelho, S. E. O'brien, E. K. Mcguire, B. M. Sanchez, G. S. Duesberg, N. Mcevoy, T. J. Pennycook, C. Downing, A. Crossley, V. Nicolosi, J. N. Coleman, et al., *Nat. Mater.* **2014**, *13*, 624.

[22] a) M. J. Large, S. P. Ogilvie, A. Amorim Graf, P. J. Lynch, M. A. O'mara, T. Waters, I. Jurewicz, J. P. Salvage, A. B. Dalton, *Adv. Mater. Technol.* **2020**, *5*, 2000284; b) P. G. Karagiannidis, S. A. Hodge, L. Lombardi, F. Tomarchio, N. Decorde, S. Milana, I. Goykhman, Y. Su, S. V. Mesite, D. N. Johnstone, R. K. Leary, P. A. Midgley, N. M. Pugno, F. Torrisi, A. C. Ferrari, *ACS Nano* **2017**, *11*, 2742.

[23] a) C. Klein, C. S. Hurlbut, J. D. Dana, *Manual of Mineralogy*, John Wiley & Sons, Inc., New York **1993** b) J. Sinkankas, *Mineralogy for Amateurs*, Van Nostrand, NewYork **1964**.

[24] a) N. Krishnamurthy, V. Soots, *Can. J. Phys.* **1971**, *49*, 885; b) B. J. Berenblut, P. Dawson, G. R. Wilkinson, *Spectrochim. Acta, Part A* **1971**, *27*, 1849.

[25] a) E. Shi, A. Wang, H. Li, R. Ogliore, Z. Ling, *J. Geophys. Res.: Planets* **2022**, *127*, e2021JE007108; b) A. M. López-Buendía, B. García-Baños, M. M. Urquiola, J. M. Catalá-Civera, F. L. Peñaranda-Foix, *Phys. Chem. Chem. Phys.* **2020**, *22*, 27713.

[26] R. K. Mishra, K. Kanhaiya, J. J. Winetrout, R. J. Flatt, H. Heinz, *Cem. Concr. Res.* **2021**, *139*, 106262.

[27] P. Ballirano, A. Maras, S. Meloni, R. Caminiti, *Eur. J. Mineral.* **2001**, *13*, 985.

[28] F. Beaugnon, J. G. D. Preturlan, F. Fusseis, E. Gouillart, S. Quiligotti, G. Wallez, *Solid State Sci.* **2022**, *126*, 106845.

[29] Y. Tang, J. Gao, C. Liu, X. Chen, Y. Zhao, *ACS Omega* **2019**, *4*, 7636.

[30] N. Prieto-Taboada, O. Gómez-Laserna, I. Martínez-Arkarazo, M. Á. Olazabal, J. M. Madariaga, *Anal. Chem.* **2014**, *86*, 10131.

[31] a) B. Lafuente, J. L. Bishop, L. K. Fenton, S. J. King, D. Blake, P. Sarrazin, R. Downs, B. H. Horgan, American Geophysical Union, **2013**, P23C-1801; b) M. S. Hossain, S. Ahmed, *RSC Adv.* **2022**, *12*, 25096.

[32] T. M. Stawski, A. E. S. Van Driessche, R. Besselink, E. H. Byrne, P. Raiteri, J. D. Gale, L. G. Benning, *J. Phys. Chem. C* **2019**, *123*, 23151.

[33] F. Sadri, R. Kim, Z. Yang, A. Ghahreman, *Hydrometallurgy* **2018**, *182*, 82.

[34] M. Maslyk, Z. Dallos, M. Koziol, S. Seiffert, T. Hieke, K. Petrovic, U. Kolb, M. Mondeshki, W. Tremel, *Adv. Funct. Mater.* **2022**, *32*, 2111852.

[35] C. Wang, X. Ma, Z. Zhang, H. Xiao, X. Zeng, J. Zhang, Z. Lin, A mesoscale self-assembly into bulk bassanite via delicate control of water activity to mimic biomineralization, Researchsquare **2022**, https://doi.org/10.21203/rs.3.rs-1508202/v1

[36] a) S. Fukugaichi, N. Matsue, *ACS Omega* **2018**, *3*, 2820; b) J. M. Galloway, Z. P. Aslam, S. R. Yeandel, A. Kulak, M. A. Ilett, Y.-Y. Kim, A. Bejarano-Villafuerte, B. Pokroy, R. M. Drummond-Brydson, C. L. Freeman, J. H. Harding, N. Kapur, F. C. Meldrum, *Chem. Sci.* **2023**, *14*, 6705.

[37] Y.-W. Wang, Y.-Y. Kim, H. K. Christenson, F. C. Meldrum, *Chem. Commun.* **2011**, *48*, 504;

[38] C. Anduix-Canto, M. A. Levenstein, Y.-Y. Kim, J. R. A. Godinho, A. N. Kulak, C. G. Niño, P. J. Withers, J. P. Wright, N. Kapur, H. K. Christenson, F. C. Meldrum, *Adv. Funct. Mater.* **2021**, *31*, 2107312.

[39] a) C. Backes, B. M. Szydlowska, A. Harvey, S. Yuan, V. Vega-Mayoral, B. R. Davies, P.-L. Zhao, D. Hanlon, E. J. G. Santos, M. I. Katsnelson, W. J. Blau, C. Gadermaier, J. N. Coleman, *ACS Nano* **2016**, *10*, 1589; b) C. Backes, T. M. Higgins, A. Kelly, C. Boland, A. Harvey, D. Hanlon, J. N. Coleman, *Chem. Mater.* **2017**, *29*, 243.

[40] C. Backes, K. R. Paton, D. Hanlon, S. Yuan, M. I. Katsnelson, J. Houston, R. J. Smith, D. Mccloskey, J. F. Donegan, J. N. Coleman, *Nanoscale* **2016**, *8*, 4311.

[41] D. Holpuch, *Spinning in Space: Centrifuge on the International Space Station*, Helmer Scientific, Noblesville, IN, US **2018**.

[42] S. De, C. S. Boland, P. J. King, S. Sorel, M. Lotya, U. Patel, Z. L. Xiao, J. N. Coleman, *Nanotechnology* **2011**, *22*, 285202

[43] C. Backes, A. M. Abdelkader, C. Alonso, A. Andrieux-Ledier, R. Arenal, J. Azpeitia, N. Balakrishnan, L. Banszerus, J. Barjon, R. Bartali, S. Bellani, C. Berger, R. Berger, M. M. B. Ortega, C. Bernard, P. H. Beton, A. Beyer, A. Bianco, P. Bøggild, F. Bonaccorso, G. B. Barin, C. Botas, R. A. Bueno, D. Carriazo, A. Castellanos-Gomez, M. Christian, A. Ciesielski, T. Ciuk, M. T. Cole, J. Coleman, et al., *2D Mater.* **2020**, *7*, 022001.

[44] C. Backes, D. Campi, B. M. Szydlowska, K. Synnatschke, E. Ojala, F. Rashvand, A. Harvey, A. Griffin, Z. Sofer, N. Marzari, J. N. Coleman, D. D. O'regan, *ACS Nano* **2019**, *13*, 7050.

[45] Y. R. Hernandez, A. Gryson, F. M. Blighe, M. Cadek, V. Nicolosi, W. J. Blau, Y. K. Gun'ko, J. N. Coleman, *Scr. Mater.* **2008**, *58*, 69.

[46] A. Harvey, C. Backes, J. B. Boland, X. He, A. Griffin, B. Szydlowska, C. Gabbett, J. F. Donegan, J. N. Coleman, *Nat. Commun.* **2018**, *9*, 4553.

[47] a) A. Abdulhameed, M. M. Halim, W. M. Wan Ahmad Kamil, K. O. Zheng, A. U. Ahmad, S. K. Alsaee, *Appl. Phys. A* **2023**, *129*, 532; b) R. Camposeco, M. Hinojosa-Reyes, R. Zanella, *Top. Catal.* **2022**, *65*, 989; c) M. M. Rahman, J. Ahmed, A. M. Asiri, I. A. Siddiquey, M. A. Hasnat, *RSC Adv.* **2016**, *6*, 90470.

[48] a) B. Lai, S. C. Singh, J. K. Bindra, C. S. Saraj, A. Shukla, T. P. Yadav, W. Wu, S. A. Mcgill, N. S. Dalal, A. Srivastava, C. Guo, *Mater. Today Chem.* **2019**, *14*, 100207; b) F. Yu, X. Jing, Y. Wang, M. Sun, C. Duan, *Angew. Chem., Int. Ed.* **2021**, *60*, 24849; c) B.-Q. Zhang, J.-S. Chen, H.-L. Niu, C.-J. Mao, J.-M. Song, *Nanoscale* **2018**, *10*, 20266.

[49] H. Nagabhushana, G. Nagaraju, B. M. Nagabhushana, C. Shivakumara, R. P. S. Chakradhar, *Philos. Mag. Lett.* **2010**, *90*, 289.

[50] S. S. Kim, T. V. Khai, V. Kulish, Y.-H. Kim, H. G. Na, A. Katoch, M. Osada, P. Wu, H. W. Kim, *Chem. Mater.* **2015**, *27*, 4222.

[51] F. Beaugnon, S. Quiligotti, S. Chevreux, G. Wallez, *Solid State Sci.* **2020**, *108*, 106399.

[52] C. Rinaudo, M. Franchini-Angela, R. Boistelle, *Mineral. Mag.* **1989**, *53*, 479.

[53] a) L. E. Brus, *J. Chem. Phys.* **1984**, *80*, 4403; b) S. Parveen, P. K. Prasanna, S. Chakraborty, P. K. Giri, *J. Mater. Chem. C* **2021**, *9*, 2437; c) H. Yu, J. Li, R. A. Loomis, L.-W. Wang, W. E. Buhro, *Nat. Mater.* **2003**, *2*, 517.

[54] a) K. F. Mak, J. Shan, *Nat. Photonics* **2016**, *10*, 216; b) Q. H. Wang, K. Kalantar-Zadeh, A. Kis, J. N. Coleman, M. S. Strano, *Nat. Nanotechnol.* **2012**, *7*, 699.

[55] J. S. Levine, M. E. Summers, *presented at 3rd* Int. Workshop on the Mars Atmosphere: Modeling and Observations, Williamsburg, Virginia, **2008**.

[56] a) J. Sanahuja, L. Dormieux, S. Meille, C. Hellmich, A. Fritsch, *J. Eng. Mech.* **2010**, *136*, 239; b) E. A. Pachon-Rodriguez, A. Piednoir, J. Colombani, *Phys. Rev. Lett.* **2011**, *107*, 146102.

[57] C. S. Boland, S. Barwich, U. Khan, J. N. Coleman, *Carbon* **2016**, *99*, 280.

[58] M. Cano, U. Khan, T. Sainsbury, A. O'neill, Z. Wang, I. T. Mcgovern, W. K. Maser, A. M. Benito, J. N. Coleman, *Carbon* **2013**, *52*, 363.

[59] P. May, U. Khan, A. O'neill, J. N. Coleman, *J. Mater. Chem.* **2011**, *22*, 1278.

[60] U. Khan, P. May, A. O'Neill, A. P. Bell, E. Boussac, A. Martin, J. Semple, J. N. Coleman, *Nanoscale* **2013**, *5*, 581.

[61] A. O'neill, U. Khan, J. N. Coleman, *Chem. Mater.* **2012**, *24*, 2414.

[62] a) R. J. Young, I. A. Kinloch, L. Gong, K. S. Novoselov, *Compos. Sci. Technol.* **2012**, *72*, 1459; b) R. J. Young, M. Liu, I. A. Kinloch, S. Li, X. Zhao, C. Vallés, D. G. Papageorgiou, *Compos. Sci. Technol.* **2018**, *154*, 110.

[63] a) D. G. Papageorgiou, I. A. Kinloch, R. J. Young, *Prog. Mater. Sci.* **2017**, *90*, 75; b) K. Hu, D. D. Kulkarni, I. Choi, V. V. Tsukruk, *Prog. Polym. Sci.* **2014**, *39*, 1934.

[64] S. C. Williams, *Tectonophysics* **1988**, *148*, 163.

[65] T. M. Stawski, H. M. Freeman, A. E. S. Van Driessche, J. Hövelmann, R. Besselink, R. Wirth, L. G. Benning, *Cryst. Growth Des.* **2019**, *19*, 3714.